

An injected quantity estimation technique based on time–frequency analysis

*Original*

An injected quantity estimation technique based on time–frequency analysis / Ferrari, Alessandro; Jin, Zhiru; Vento, Oscar; Zhang, Tantan. - In: CONTROL ENGINEERING PRACTICE. - ISSN 0967-0661. - ELETTRONICO. - 116:(2021), p. 104910. [10.1016/j.conengprac.2021.104910]

*Availability:*

This version is available at: 11583/2918192 since: 2022-12-13T08:56:28Z

*Publisher:*

Elsevier

*Published*

DOI:10.1016/j.conengprac.2021.104910

*Terms of use:*

This article is made available under terms and conditions as specified in the corresponding bibliographic description in the repository

*Publisher copyright*

Elsevier postprint/Author's Accepted Manuscript

© 2021. This manuscript version is made available under the CC-BY-NC-ND 4.0 license  
<http://creativecommons.org/licenses/by-nc-nd/4.0/>. The final authenticated version is available online at:  
<http://dx.doi.org/10.1016/j.conengprac.2021.104910>

(Article begins on next page)

# An injected quantity estimation technique based on time-frequency analysis

Ferrari Alessandro <sup>(\*)</sup>,<sup>1</sup>, Jin Zhiru<sup>1</sup>, Vento Oscar<sup>1</sup> and Zhang Tantan<sup>1</sup>

<sup>1</sup>Energy Department

Politecnico di Torino, Corso Duca degli Abruzzi 24, 10129, Torino, Italy

(\*) Corresponding author. Email: [alessandro.ferrari@polito.it](mailto:alessandro.ferrari@polito.it) Phone +390110904426

## 1. Abstract

An innovative injected quantity estimation method, based on time-frequency analysis, has been developed for passenger car Common-Rail (CR) injection systems. This method involves capturing the pressure time history from a transducer installed along the rail-to-injector pipe, and its overall accuracy has been found to be within 1.5 mg.

The dependence of the injected mass on the fuel temperature has been investigated, and the correlation of the injected mass with the nominal rail pressure and the energizing time has been evaluated for different thermal regimes. It has been verified that if the duration of the hydraulic injection is considered instead of the energizing time, the influence of the temperature on the injected mass is implicitly taken into account. Thus, the corresponding correlations between the injected mass and the duration of the hydraulic injection have been obtained for different nominal rail pressures.

The duration of the hydraulic injection has been measured through an effective time-frequency analysis technique, which has been used to realize a virtual sensor of the needle lift.

The experimental campaign has been performed over a wide range of working conditions for single injections, and the accuracy of the innovative prediction methodology, which can be exploited to design a closed-loop control of the injected mass, has been assessed.

## 2. Keywords

Common-rail, time-frequency analysis, injected mass estimation, fuel injection system

### 25        **3. Highlights**

- 26    -        A correlation between the injection temporal length and injected mass is obtained.
- 27    -        Nozzle opening and closure are detected by means of a virtual needle-lift sensor.
- 28    -        The injected mass is predicted from a pressure trace measured at the injector inlet.

### 29        **1. Introduction**

30    Internal combustion engines require continuous development [1], due to the demand for improved  
31    performances with increased fuel economy and in order to comply with stringent emission legislations  
32    [2, 3]. In addition to the design of new technologies, researchers have been focusing on fault detection  
33    and diagnosis of the system [4, 5, 6] to fulfill these requirements.

34    In-cylinder pressure measurements and analyses have played important roles in the field of diagnosis  
35    and real time monitoring [7, 8]. The main features of the combustion process can be identified and  
36    evaluated by analyzing an accurately processed pressure signal. Investigations of this kind include the  
37    detection and control of the start of combustion [9, 10], of the heat release rate [11] as well as of knock  
38    and misfire phenomena [12, 13]. Similarly, empirical models have been established to determine the  
39    ignition delay [14] and the barycenter of combustion [15].

40    Time-frequency analysis (TFA), a powerful tool that may be used to analyze non-stationary signals [16],  
41    has been applied to detect and diagnose machinery faults [17, 18]. This advanced technique has also  
42    been proposed to study combustion and knock in diesel engines by evaluating the vibration signals in  
43    these engines [6, 19]. Among the various techniques that are available, short-time Fourier transform  
44    (STFT) is generally applied to characterize signals in the time-frequency domain. It is possible, for  
45    example, to estimate such characteristic combustion parameters as the peak combustion pressure and  
46    peak pressure rise rate through the vibration signal [20]. An estimation of the trapped mass was carried  
47    out in [21, 22] by means of an analysis of the in-cylinder pressure resonance.

48    The detection of vibration sources, by means of STFT, was proposed in [23] for mechanical systems.  
49    The main events of an injection, that is, the opening and the closure of the nozzle, were identified in [24]  
50    by analyzing the pressure signal from a diesel engine fuel injection apparatus.

51 One topic of great interest in the real-time monitoring of diesel engines is related to the accurate control  
52 of the mass injected into diesel injection systems. Different advanced compensative strategies have  
53 been set up by injection apparatus suppliers: i-ART, presented by Denso [25], NCS, proposed by Bosch  
54 [26] and the Switch technology by Delphi [27]. With these techniques, semi-empirical correlations or  
55 transfer functions are implanted in the electronic control unit (ECU), and specific signals are captured  
56 and used to estimate the injected quantity. The nominal rail pressure ( $p_{nom}$ ) or the energizing time ( $ET$ )  
57 can then be compensated for by comparing the estimated injected mass value and the target value.  
58 However, such compensative strategies can only ensure an improvement in the accuracy of the injected  
59 mass for those engine working conditions for which the correlations fit. In fact, the usage of a transfer  
60 function is not founded on a physical basis, since the injector cannot be modeled by means of ordinary  
61 differential equations of time invariant coefficients. In general, one of the main drawbacks of engine  
62 calibrations of the injected mass is represented by the thermal regime: the calibrations are usually  
63 prepared with the injection system installed on the hydraulic rig under certain temperature conditions,  
64 and they can result inaccurate for many thermal regimes experienced in the engine. This is the main  
65 discrepancy that requires compensation. On the one hand, a reliable and accurate correction of the  
66 injected mass, with respect to the thermal regime of the engine, is very difficult to realize. On the other  
67 hand, such a correction could lead to clear benefits, in terms of the reduction in soot (6%),  $NO_x$  (3÷4%)  
68 engine out emissions and  $CO_2$ , as well as in combustion noise (as much as 5 dB) and fuel consumption  
69 [28, 29].

70 In the present work, a new correlation has been developed between the injected mass, the nominal rail  
71 pressure and the injection temporal length ( $ITL$ ) to design a robust, original, closed-loop control of the  
72 injected mass.  $ITL$  has been determined by means of a previously developed, TFA-based, virtual sensor  
73 of the needle lift [24]. The introduction of  $ITL$  into the correlation allows the thermal regime of the  
74 injector to be included in the prediction of the injected mass.

## 75 **2. Time-frequency analysis**

76 TFA integrates the techniques that study signals in both the time and the frequency domains in order to  
77 indicate the changes in the frequency spectrum of a transient signal  $f(t)$ . In the present work, the focus

78 has been on the changes in the nozzle opening and closure instants. A great number of fast Fourier  
79 transforms (FFT) are performed over consecutive, overlapping, short-time ranges, and each FFT result  
80 refers to the mean instant of the time interval. The non-stationary signal is assumed to refer to a  
81 stationary performance within each time interval, and a local frequency spectrum is therefore obtained.  
82 From an operative point of view, a windowing of signal  $f(t)$  is carried out: signal  $f(t)$  is multiplied by a  
83 selected window function  $h(t-\tau)$ , which is of unit energy and is only non-zero over an interval around  
84 instant  $\tau$ . The short-time Fourier transform (STFT) is then evaluated as follows:

$$85 \quad F(\nu, \tau) = \int_{-\infty}^{+\infty} f(t) \cdot h(t - \tau) e^{-j2\pi\nu t} dt \quad (1)$$

86 Since the selected window function does not introduce any energy variation, the energy density  
87 spectrum  $P_f$  of signal  $f$  is obtained in the following way:

$$88 \quad P_f(\nu, \tau) = |F(\nu, \tau)|^2 \quad (2)$$

89 The energy of signal  $f$ , denoted as  $E_f$ , is given by

$$90 \quad E_f = \int_{-\infty}^{+\infty} \int_{-\infty}^{+\infty} P_f(\nu, \tau) d\tau d\nu \quad (3)$$

91 The energy density spectrum  $P_f$  can be interpreted as a probability density function to evaluate the  
92 following mean instantaneous frequency (*MIF*):

$$93 \quad \bar{\nu}(\tau) = \frac{1}{\int_{-\infty}^{+\infty} P_f(\nu, \tau) d\nu} \int_{-\infty}^{+\infty} \nu \cdot P_f(\nu, \tau) d\nu \quad (4)$$

94 Hence, the *MIF* can be interpreted as the most representative frequency of a signal at a certain time  
95 instant.

### 96 **3. Experimental setup**

97 The experimental campaign has been conducted on a Moehwald-Bosch hydraulic test bench installed in  
98 the ICE laboratory at the Politecnico di Torino. The bench is capable of providing a nominal power of  
99 35 kW, a maximum torque of 100 Nm and a maximum speed of 6100 rpm. As reported in Fig. 1, the  
100 injection rate and the injected quantity that refer to the injector under analysis were captured by means  
101 of a Zeuch method-based flowmeter (HDA from Moehwald-Bosch) [30]. The electric current supplied  
102 to the injector was measured by means of a current clamp. Furthermore, one piezoresistive pressure  
103 transducer was mounted along the rail-to-injector pipe of the CR system in order to acquire the pressure

104 time history at the electroinjector inlet ( $p_{inj}$ ). Finally, a PXI (from National Instruments) was connected  
105 to the output of the pressure transducer in order to collect  $p_{inj}$  at a sample frequency of 500 kHz.

106 A state-of-the-art Bosch fuel injection system for passenger cars has been tested. A high-pressure rotary  
107 pump, with a double-effect single piston and a total displacement of 430 mm<sup>3</sup>/rev, is employed in the  
108 system. Bosch CRI 2.18 solenoid-actuated injectors (cf. Fig. 2), which feature a pressure balanced  
109 pilot-valve at the exit of the control chamber, were installed.

110 A schematic of the hydraulic circuit of the injection system from the rail onward is reported in Fig. 3.  
111 When the injection system is operating, high-pressure fuel, supplied by the pump to the rail, enters the  
112 injector through a rail-to-injector pipe. A small quantity of the fuel arrives in the control chamber (cf.  
113  $V_{cc}$  in Fig. 3), while the rest fills the delivery chamber, located upstream of the injection holes. When the  
114 electrical current is supplied to the solenoid, the pilot-valve is open and the fuel pressure in the control  
115 chamber reduces, because of the fuel recirculated to the tank. The needle ascends, due to an imbalance  
116 of the pressure forces that act on its working surfaces, and the nozzle opens, thus allowing the fuel to be  
117 injected through the injection holes. When the current is shut down by the ECU, the closure of the  
118 pilot-valve makes the pressure rise in the control chamber, and this results in a downstroke of the needle.  
119 As soon as the needle arrives at its initial position, the injection holes close again.

120 Shell V-Oil 1404 (ISO 4113) calibration fluid is employed at the hydraulic test bench, because it  
121 reproduces the physical properties of diesel oil over an adequate pressure and temperature range.

122 Tests were carried out considering single injections, featuring  $p_{nom}$  over the 500-1700 bar range, and  
123  $ET$  over the 0.35-1.1 ms range, with oil temperatures, measured at the fuel tank, equal to either  
124  $T_{tank}=40$  °C or 68 °C.

125 All the experimental tests of the present work were conducted at a fixed pump speed of 2000 rpm,  
126 which corresponds to an engine speed of 2000 rpm (the pump-to-engine speed ratio is 1:1). Since the  
127 pump speed does not exert any significant influence on the CR performance, the obtained results can be  
128 generalized to other engine speeds.

#### 129 **4. Injector characteristics**

130 Figure 4 reports the values of the injected mass, measured by means of the HDA flowmeter, as an

131 average of 100 consecutive engine cycles for different  $p_{nom}$  and  $ET$ . The temperature of the fuel in the  
132 tank ( $T_{tank}$ ) was set either at 40 °C (cf. circle symbols and dashed lines) or at 68 °C (cf. square symbols  
133 and continuous lines). In fact, diesel fuel injection system suppliers usually assume a reference  
134 temperature of 40 °C for hydraulic tests. Furthermore, the 68 °C value corresponds to the maximum  
135 temperature that can be reached on the current test bench (a limit of around 70 °C is common on  
136 hydraulic test benches for safety reasons). The  $M_{inj}$  versus  $ET$  curves for each  $T_{tank}$  and  $p_{nom}$  value are  
137 fitted by a third-order polynomial. The fuel velocity through the nozzle can in fact be considered a  
138 function of  $p_{nom}$  and  $T_{tank}$ , and the same occurs for the density. Since the restricted flow area at the nozzle  
139 is a quadratic function of the needle lift and the needle-lift peak value can be considered to grow  
140 proportionally with  $ET$  (the needle is ballistic and the needle lift time history has a triangular shape), the  
141 mean injected flow-rate can be regarded as a quadratic polynomial function of  $ET$  at fixed  $p_{nom}$  and  $T_{tank}$   
142 and the injected mass as a cubic function of  $ET$  at fixed  $p_{nom}$  and  $T_{tank}$ . Figure 5 reports the trend of the  
143 mean injected flow-rate, namely  $\overline{G_{inj}}$ , with respect to  $ET$  for three different nominal rail pressures at  
144  $T_{tank} = 40$  °C (the polynomial coefficients of the interpolating curves are listed in the graph). As can be  
145 inferred, the experimental data of  $\overline{G_{inj}}$  correlate well with quadratic polynomials and the contribution  
146 of the second order term is not marginal compared to the contribution of the linear term.

147 The injected mass grows as  $T_{tank}$  increases under fixed  $p_{nom}$  and  $ET$  values. Furthermore, the lower the  
148 rail pressure is, the higher the difference between the injected masses when  $T_{tank}$  is changed. Figs. 6a and  
149 6b report some  $ET$  sweeps of injected mass flow-rate ( $G_{inj}$ ) patterns pertaining to  $p_{nom}=800$  bar and  
150  $p_{nom}=1600$  bar, respectively.  $G_{inj}$  time histories at  $T_{tank}=40$  °C and 68 °C are compared in each graph. The  
151 injected flow-rate at  $p_{nom} = 800$  bar is controlled more by the needle seat passage than at  $p_{nom} = 1600$  bar.  
152 In fact, the higher  $ET$  in Fig. 6a is, the higher the needle lift peak value and the higher the injected  
153 flow-rate peak value; this does not occur at  $p_{nom} = 1600$  bar (cf. Fig. 6b), where the flow-rate is mainly  
154 controlled by the nozzle injection holes and therefore, independently of the peak value of the needle lift,  
155 which increases with  $ET$  (the injector is ballistic), the maximum  $G_{max}$  value remains constant. All this  
156 justifies a greater impact of the needle lift time history on the injected flow rate time history, when  
157  $p_{nom}=800$  bar. Since a temperature increase determines a reduction in the fuel viscosity [31] and a

158 subsequent diminution in the friction stresses [32] acting on the needle, the thermal effect on the  
159 injected mass is more obvious at  $p_{nom}=800$  bar than at  $p_{nom}=1200$  bar or  $p_{nom}=1600$  bar. From the  
160 comparison of the data obtained at  $T_{tank}=40^{\circ}\text{C}$  and  $T_{tank}=68^{\circ}\text{C}$ , it has been possible to analyze  
161 sufficiently the investigated effect: the predominant effect of the fuel temperature on the injector  
162 dynamics is the reduced friction force acting on the needle and this is in line with what determined in  
163 [33] for higher injector inlet temperatures than  $0^{\circ}\text{C}$ .

164 It can be observed, from the data reported in Fig. 4, that when  $p_{nom}=800$  bar and  $ET=800\ \mu\text{s}$  are applied  
165 ( $M_{inj}\approx 25$  mg at  $T_{tank}=40^{\circ}\text{C}$ ), the difference in the injected quantity between the two considered  
166 temperatures of the fuel in the tank can reach a value close to 3 mg. Furthermore, the injection  
167 temperature variation can generally be higher when the injection system, installed on the engine,  
168 undergoes different thermal regimes than when it is tested at the hydraulic rig, first at  $T_{tank}=40^{\circ}\text{C}$  and  
169 then at  $T_{tank}=68^{\circ}\text{C}$ .

170 Accurately determining thermal regimes in the nozzle of an injector during operations on an engine is a  
171 complex procedure [34]: the fuel temperature at the injector inlet grows, in comparison to  $T_{tank}$ , at a rate  
172 of about  $1^{\circ}\text{C}$  for every 100 bar of pump compression, and most of the temperature increase occurs  
173 through the injector. However, for the purpose of the present analysis, it was sufficient to characterize  
174 the thermal regime with the controllable temperature of the fuel in the tank. Indeed, the injected  
175 flow-rate is sensitive to  $T_{tank}$ . The start of injection (*SOI*) occurs at almost the same time instant as  $T_{tank}$   
176 changes (cf. Figs. 5a and 5b), but the flow-rates pertaining to the lower temperature start to decrease  
177 earlier, thereby advancing the end of injection (*EOI*). *ITL* can be expressed as

$$178 \quad \quad \quad ITL = EOI - SOI \quad \quad \quad (5)$$

179 which is the time interval during which the instantaneous injected flow-rate  $G_{inj}$  is higher than zero, as  
180 indicated in Fig. 6 with reference to  $ET = 700\ \mu\text{s}$  (for other  $ET$  values *ITL* is defined in the same way). It  
181 is observed that for increasing  $T_{tank}$ , *ITL* enlarges. As a consequence, when  $p_{nom}$  is fixed and the fuel  
182 temperature rises, the correlation between the injected mass and  $ET$  shifts, in line with the data shown in  
183 Fig. 4.

184 Third-order polynomial fitting of the *ITL*- $M_{inj}$  data was conducted for each  $p_{nom}$  and the correlations are  
185 plotted in Fig. 7. As can be inferred, the correlation between *ITL* and  $M_{inj}$  remains for fixed  $p_{nom}$  as  $T_{tank}$

186 varies from 40 °C to 68 °C. Thus, it can be observed that the  $ITL$ - $M_{inj}$  correlation is almost independent  
187 of the fuel temperature. This suggests the possibility of determining  $M_{inj}$  on the basis of the  
188 experimental  $p_{nom}$  and  $ITL$  values, independently of  $T_{tank}$ , which leads to a more robust correlation than  
189 the common one implemented on the ECU, namely  $M_{inj}=f(ET, p_{nom})$ .

## 190 **5. Implementation of the TFA injection duration sensor**

191 Figure 8 shows the  $G_{inj}$ ,  $p_{inj}$  and the energizing current traces pertaining to  $p_{nom}=1200$  bar and  $ET=600$   
192  $\mu$ s. The reported traces correspond to average values over 100 consecutive engine cycles. No obvious  
193 residual pressure waves are present in the hydraulic circuit before the injection starts: therefore,  $p_{inj}(t)$   
194 remains almost horizontal. As the energizing current is activated, a slight reduction in  $p_{inj}$  takes place,  
195 due to the opening of the pilot-valve and, as soon as the effective injection starts ( $SOI$ ), an expansion  
196 wave is triggered, and this causes a significant decrease in  $p_{inj}$  (marked 1 in Fig. 8). The stimulated  
197 rarefaction waves are reflected at the rail and propagate backward and forward along the rail-to-injector  
198 pipe, and this results in fluctuations of  $p_{inj}$  with respect to the time. The amplitude of the  $p_{inj}$  oscillations  
199 remains pronounced over the entire injection phase, although they are gradually damped by wall  
200 friction along the rail-to-injector pipe and by concentrated losses. As soon as the hydraulic injection  
201 phase finishes ( $EOI$ ), the closure of the nozzle induces a water hammer with an evident rise and final  
202 peak in  $p_{inj}$  (event marked 2 in Fig. 8).

203 The time instants that refer to the important changes in  $p_{inj}$  (cf. 1 and 2 in Fig. 8) are linked to the  
204 corresponding hydraulic events ( $SOI$  and  $EOI$ ). However, the determination of the exact time instant at  
205 which the decrease in  $p_{inj}$  pertaining to  $SOI$  really starts is not an easy task, since any pressure disturbing  
206 variation can affect the detection. Similar problems are encountered for the determination of  $EOI$ . In  
207 fact, reflected pressure waves traveling along the rail-to-injector pipe can influence the  $p_{inj}$  time history,  
208 thus making the capture of the  $EOI$  misleading.

209 TFA can be a useful tool to apply to  $p_{inj}$  in order to extract well-resolved information on  $SOI$  and  $EOI$  for  
210 the estimation of the final injected mass. In general, the  $SOI$  and the  $EOI$  of the same injector are  
211 concentrated within a time span of 4 ms. In order to locate those time instants with TFA and to avoid any  
212 leakage errors (these are given by spurious harmonic terms that are generated when only a portion of a

213 periodic signal is considered [35]), ascribable to the start and the end of the signal, a sequence of  $p_{inj}(t)$   
 214 frames, each with a total length of 8 ms, has been taken as the signal on which  $MIF$  is evaluated.  
 215 In order to smooth the experimental  $p_{inj}$  signal, it was preliminarily treated with a Butterworth low-pass  
 216 filter of the fourth order with a cut-off frequency of 50 kHz. The thus processed signal, namely  $p_{inj,fil}$ ,  
 217 was used to substitute  $f(t)$  in Eq. (1). A Hanning window was selected as the window function employed  
 218 in Eq. (1):

$$219 \quad h(n) = 0.5 \left( 1 - \cos\left(2\pi \frac{n}{N}\right) \right), 0 \leq n \leq N \quad (6)$$

220 where  $n$  stands for a discretized time instant in the window, and  $N+1$  is the window length (duration) in  
 221 terms of number of samples. In the present work, a window length of 502  $\mu$ s was chosen. Provided that  
 222 the sample frequency of  $p_{inj}$  is 500 kHz,  $N$  will be equal to 251. By applying these parameters and  
 223 conditions, the STFT of  $p_{inj}$  is obtained via Eq. (1), and  $MIF$  can then be calculated by means of Eqs. (2)  
 224 and (4).

225 It must be noticed that the sample frequency may be reduced around 20 kHz without any criticism. This  
 226 value is able to contain almost all the energy content of the pressure signal frequency spectrum [36],  
 227 leading to a remarkable reduction of the computational time.

## 228 **6. Results**

229 Figures 9-11 plot the electrical current, as well as the  $G_{inj}$ ,  $p_{inj}$  and  $MIF$  time histories for three different  
 230 working conditions of  $p_{nom}$  and  $ET$  over a time interval of 4 ms, where  $T_{tank}$  was set to 40 °C. The  $MIF$   
 231 trace in the plots takes on a constant value before the electrical start of the injection has occurred, but  
 232 this initial level is not visible in the graphs because it is a too large value, due to the leakage error.  
 233 By analyzing the  $MIF$  trace referring to the pressure at the injector inlet, the main impulsive events  
 234 regarding the injection can be detected. The  $MIF$  time history is sensitive to the needle movements, and  
 235 both the beginning of its ascendent phase (when the injection starts) and the end of the descending phase  
 236 (when the injection ends) can be identified with high resolution as quick changes in the  $MIF$  value. The  
 237 first local maximum in the  $MIF$  diagram (related to nozzle opening, marked as 1 in Figs. 9-11) can be  
 238 estimated as the hydraulic start of injection ( $SOI$ ), which takes place around 0.1 ms after the effective  
 239 instant at which the nozzle opens, and  $G_{inj}$  thus becomes higher than zero (cf. Figs. 9-11). Such a delay

240 is necessary for the rarefaction wave that is triggered by the injection to propagate from the nozzle to the  
241 pressure transducer location [24]. Similarly, the time instant at which the absolute maximum value of  
242  $MIF$  (related to the water hammer at the end of the injection event) occurs, that is, at about 0.1 ms after  
243 the end of the hydraulic injection, was considered as the  $EOI$ . It has been seen that this criterion holds  
244 for all the working points examined in the experimental campaign for both  $T_{tank} = 40$  °C and  $T_{tank} =$   
245 68 °C.

246 The  $MIF$  estimated injection duration ( $ITL_{est}$ ) and the real one, namely  $ITL$ , were in turn calculated by  
247 means of Eq. (5), and with the corresponding experimental data referring to  $MIF$  and injected flow rate,  
248 respectively. Since similar delays occur at both the start and the end of  $ITL_{est}$ ,  $ITL$  and  $ITL_{est}$  can be  
249 considered as coincident. As can be inferred from the legends in Figs. 9 and 10, the errors between  
250  $ITL_{est}$  and  $ITL$  are 1.49  $\mu$ s and 5.71  $\mu$ s, respectively (percentage errors below 1%).

251 Figure 11 plots the same quantities as those shown in Figs. 9 and 10 for the  $p_{nom}=600$  bar and  $ET= 1000$   
252  $\mu$ s case. The instants, estimated as  $SOI$  and  $EOI$  with the support of  $MIF$ , feature a time delay of around  
253 0.18 ms with respect to the real values. However, when the  $G_{inj}$  trace is considered, the error between  
254  $ITL$  and  $ITL_{est}$  is 90.74  $\mu$ s, which is much higher than in Figs. 9 and 10. This alteration occurs for very  
255 large ET values and may be due to the superposition of the rail reflected waves and the water hammer  
256 along the rail-to-injector pipe ( $ET = 1000$   $\mu$ s is not usually applied for this injector setup).

257 The calculated  $ITL_{est}$  data shown in Fig. 9 and Fig. 10 were applied to the correlation reported in Fig. 7,  
258 and values of the estimated injected mass ( $M_{inj,est}$ ) equal to 30.84 mg and 16.01 mg were predicted,  
259 respectively. If a comparison with the corresponding  $M_{inj}$  data evaluated by means of the HDA  
260 flowmeter is made, the errors in the prediction of the injected mass are well below 0.5 mg, which can be  
261 considered a very satisfactory result. For the case in Fig. 11,  $M_{inj,est}$  is 27.56 mg and there is a difference  
262 of 1.2 mg, compared to the  $M_{inj}$  value of the HDA flowmeter.

263 The estimated injected mass has been evaluated for various steady-state working conditions, in terms of  
264  $p_{nom}$  and  $ET$ , by means of the developed correlation, based on the TFA methodology. The modulus of the  
265 difference between  $M_{inj,est}$  and  $M_{inj}$ , that is, the prediction accuracy  $|AM_{inj}|$ , is reported as the vertical  
266 ordinate in the 3D diagrams in Fig. 12 as a function of  $p_{nom}$  and  $ET$ . The fuel temperature,  $T_{tank}$ , was set

267 at 40 °C (cf. Fig. 12a) and at 68 °C (cf. Fig. 12b). The  $M_{inj}$  values were measured, by means of the HDA  
268 flowmeter, and they correspond to average values of over 100 consecutive engine cycles. Since the  
269 maximum injected mass per engine cycle is below 45 mg for the considered application involving these  
270 injectors, the range over which both  $p_{nom}$  and  $ET$  were high was excluded from the experimental  
271 campaign. The accuracy is generally within 1 mg for over 80% of the explored working conditions.  
272  $|\Delta M_{inj}|$  can reach values close to 1.5 mg for either  $500 \text{ bar} \leq p_{nom} \leq 600 \text{ bar}$  and medium and high  $ET$   
273 values with  $T_{tank}$  at both 40 °C and 68 °C or for  $350 \mu\text{s} \leq ET \leq 450 \mu\text{s}$  and high  $p_{nom}$  values when  $T_{tank}$  is  
274 equal to 40 °C. The injected mass percentage errors under the two considered fuel temperature values  
275 have also been evaluated and are reported in Fig. 13 (cf. Fig. 13a for  $T_{tank} = 40 \text{ °C}$  and Fig. 13b for  $T_{tank}$   
276 = 68 °C). When the injected masses are small for both the fuel tank temperatures, a small absolute error  
277 (even if it is smaller than 1 mg) can lead to a percentage error up to 15%, which is an acceptable value.  
278 Preliminary tests were also performed on double injections (pilot-main injections). In such a case, it is  
279 difficult to evaluate  $ITL$ , due to the numerous events that affect  $p_{inj}$ , especially when the dwell time  
280 between the consecutive injections is reduced. The present methodology can be used to control the mass  
281 injected during the first pilot injection of the multiple injection train, and this can lead to benefits in  
282 terms of reductions in soot and  $\text{NO}_x$  engine out emissions, as well as in combustion noise. Similarly, the  
283 strategy could be applied to control the main fuel shot of a main-after injection schedule.

## 284 6. Discussion

285 The new applied transfer function appears to be more simple and direct than the compensative strategies  
286 mentioned in Sect. 1, where different steps are required: based on a measured pressure signal, the needle  
287 lift is deduced and this outcome is then used in the prediction of the injected flow-rate, which is finally  
288 integrated to estimate the injected mass. The presented technique is not invasive from the injector point  
289 of view, it can be applied to different injector types without any modification in the injector internal  
290 layout.

291 It is worth observing that there are two contributions to the  $|\Delta M_{inj}|$  error. The first is the error introduced  
292 by the correlation; although the fitting technique is satisfactory, with an accuracy within 0.5 mg, this  
293 contribution is not negligible for state-of-the-art injection systems. The second contribution, which is

294 the predominant one, is the error in the estimation of  $ITL$  due to the superposition of the pressure waves.  
295 The injected flow rate not only depends on the rail pressure (which is controlled in the  $CR$  system), but  
296 also on the needle dynamics. The latter aspect is only taken into account roughly in standard engine  
297 calibrations, because they make use of  $ET$ , which, as has been shown, can differ significantly from the  
298 effective injection duration. The implementation of the correlation between the injected mass and  $ITL$   
299 for different  $p_{nom}$  on the engine ECU maps improves the consistency of the  $M_{inj}$  interpolation model,  
300 because  $ITL$  is more closely related to the needle lift than  $ET$ . Furthermore, the application of  $ITL$  as an  
301 independent variable of the correlation allows the thermal effect of the injector to be included in the  
302 prediction of the injected mass: this is a fundamental point, as may be observed in Fig. 4, since the  
303 thermal regime significantly influences the injected mass at fixed values of  $ET$  and  $p_{nom}$ .

304 From the injector characteristics (cf. Fig. 4), at  $T_{tank}=40^{\circ}\text{C}$ , the injected mass is smaller than 3 mg for  
305  $p_{nom} \leq 800$  bar and  $ET = 350$   $\mu\text{s}$  (for a pilot injection the injected mass is usually below this value).  
306 Under these working conditions, the percentage error on the fuel estimated mass with the closed loop  
307 control is below 15% (cf. Fig. 13) for both  $40^{\circ}\text{C}$  and  $68^{\circ}\text{C}$  (this is an optimum value for injected masses  
308 below 10 mg), while this error can arrive at 25% if the temperature increase from  $40^{\circ}\text{C}$  to  $68^{\circ}\text{C}$  and an  
309 open-loop control is adopted. Furthermore, if a low temperature combustion is considered, the pilot  
310 injected quantity can be increased till 7-8 mg [37]: in this case, the percentage error on the  $M_{inj}$   
311 estimation at  $T_{tank}=68^{\circ}\text{C}$  is in the 2%-15% range (cf. Fig. 13), while becomes higher than 30% for the  
312 open loop control. In this way, in the presence of a multiple injection strategy, the injected mass control  
313 could be implemented to the first pilot injection. Moreover, further efforts are needed to accurately  
314 filter the  $MIF$  time history, in order to remove the disturbances due to pressure waves, and to be able to  
315 efficiently apply the procedure to multiple injections with reduced dwell times. This represents a  
316 possible future step in the development of the new control strategy. In addition, the same strategy could  
317 be applied to control the late phased post injection for DPF regeneration.

318 Figure 14 reports the scheme of a possible closed-loop control strategy based on the presented  
319 technique, that could be applied cycle-by-cycle. The  $ITL$  is estimated based on the measured  $p_{inj,in}$   
320 through the TFA virtual sensor. The  $ITL$  estimation and the nominal rail pressure level  $p_{nom}$  can then be

321 used to evaluate the injected mass ( $M_{inj,est}$ ). Such a value is compared with the injected mass target  
322 ( $M_{inj,ref}$ ), stored in the *ECU* maps and the difference, namely  $\varepsilon = M_{inj,ref} - M_{inj,est}$ , is the input value to a  
323 *PID* controller in order to correct the *ET* value sent to the injector. The determined correction can be  
324 applied to the next injection cycle.

325 In [28,29], it has been proved the effectiveness of the application of a feedback signal to correct the *ET*  
326 in order to mitigate the error led by the thermal regime of the engine. As has been already assessed [28],  
327 a closed-loop control of the injected mass, based on cycle-to-cycle *ET* correction, is generally able to  
328 maintain the repeatability of the fuel dosage achieved under a standard open-loop strategy, that is below  
329 10% for all the considered cases for a state-of-the-art injector [28]. In other words, the proposed closed  
330 loop should improve the accuracy of the injected mass without affecting its precision. It is challenging  
331 to improve the elevated precision of the open-loop control because it is based on the severe tolerances  
332 applied to the injector manufacturing process and, moreover, the closed loop control is more aimed at  
333 compensating physical effects (due to thermal regime) than cycle-to-cycle dispersion (due to stochastic  
334 phenomena). In order to achieve the latter objective, the accuracy of the *ITL* vs.  $M_{inj}$  correlation should  
335 be further improved (the error should be below 0.5 mg), but this appears a difficult task.

336 The actual technology would in principle need a pressure sensor placed near to each injector inlet along  
337 the rail-to-injector pipes (contrarily to the strategies presented in [28,29], where two sensors are  
338 required). However, since the differences in  $M_{inj}$  are due to the injector thermal regime and are therefore  
339 based on a physical phenomenon, the same correction, evaluated for one injector, can be applied to the  
340 other injectors by taking into account the injector-to-injector dispersion. The latter is considered in the  
341 *ECU* maps by means of special injector codes that further correct the nominal *ET* for each injector.  
342 Hence, a single pressure sensor applied at the inlet of one of the injectors is expected to be enough for  
343 the multi-cylinder engines.

344

## 345 **7. Conclusions**

346 A closed-loop control of the injected mass would be a valuable innovation for designing cleaner and  
347 more efficient diesel engines.

348 A method for a real-time estimation of the injected mass has been designed by applying a TFA  
349 technique to the pressure time history measured at the injector inlet and the reliability of the method has  
350 been assessed on single injections.

351 The dependence of the injected mass on the thermal regime of the injector has been preliminarily  
352 investigated by varying  $T_{tank}$  at fixed  $p_{nom}$  and  $ET$ : the difference in the corresponding injection rate  
353 patterns is mainly related to  $ITL$ . When  $p_{nom}$  is fixed and  $ITL$  is employed as the controlled variable  
354 instead of  $ET$ , an accurate correlation of  $M_{inj}$  can be obtained with  $ITL$ , which is independent of  $T_{tank}$ .

355 A TFA-based virtual sensor of the needle lift, which was presented in a previous work, has then been  
356 assessed and further developed in order to estimate the  $ITL$ . The  $MIF$  trace, obtained from the pressure  
357 signal measured at the injector inlet, is the key to capturing the two time instants that are used to obtain  
358  $ITL_{est}$ . The injection duration is evaluated by monitoring the first  $MIF$  peak after the energizing current  
359 (which is related to the nozzle opening) and the absolute maximum of the  $MIF$  (related to the water  
360 hammer at the end of the injection event). Hence, thanks to these points,  $ITL_{est}$  can be determined.

361 Finally, the  $M_{inj,est}=M_{inj,est}(p_{nom}, ITL_{est})$  correlations have been used to predict the injected mass for an  
362 extended working condition range of the injection system (in terms of  $p_{nom}$ ,  $ET$  and  $T_{tank}$ ): for single  
363 injections, the observed accuracy of the algorithm results to be below 1.5 mg for all the considered cases,  
364 and within 1 mg for most of them. Two different sources of error affect the injected mass estimation: the  
365 first is related to the  $ITL$ - $M_{inj}$  correlation and the second is associated with the inaccuracy of  $ITL_{est}$ .

366 The presented method can be applied to design a closed-loop control strategy of the injected mass for  
367 single injections or to control the mass injected during the first injection of a multiple injection schedule.  
368 This can help to minimize the well-known inaccuracy that can be observed when a calibration  
369 conducted at a hydraulic bench is used in the engine, where different thermal conditions can be  
370 experienced. A scheme for the implementation of the closed loop control has been reported: difference  
371  $M_{inj,ref} - M_{inj,est}$  is used as an input value to a PID-controller in order to correct the  $ET$  of the next injection  
372 cycle.

## 373 8. Nomenclature

374 CR Common Rail

375	$E$	signal energy
376	$ET$	energizing time
377	ECU	electronic control unit
378	$EOI$	end of injection
379	FFT	fast Fourier transform
380	$FMV$	fuel metering valve
381	$G$	mass flow-rate
382	$h$	window function
383	$ITL$	injection temporal length
384	$n$	discretized time instant
385	$M$	fuel mass
386	$MIF$	mean instantaneous frequency
387	$P$	energy density spectrum
388	$p$	fuel pressure
389	$PCV$	pressure control valve
390	$P/E$	pressure sensor
391	$SOI$	start of injection
392	STFT	short-time Fourier transform
393	$T$	fuel temperature
394	$t$	time
395	TFA	time-frequency analysis
396	$\varepsilon$	error on the injected mass
397	$\nu$	frequency
398	$\tau$	time
399	<u>Subscripts</u>	
400	$0$	reference
401	$cc$	control chamber

402 *est* estimated  
403 *inj* injected, injector  
404 *nom* nominal  
405 *tank* tank

## 406 **9. References**

- 407 [1] BS. Dooren, C. Balerna, M. Salazar, A. Amstutz, C. Onder, Optimal Diesel Engine Calibration using  
408 Convex Modelling of Pareto Frontiers, *Control Engineering Practice* 96 (2020) 104313.
- 409 [2] Z. Liu, A. DizqahS, J. Herreros, J. Schaub, O. Haas, Simultaneous Control of NOx, Soot and Fuel  
410 Economy of a Diesel Engine with Dual-loop EGR and VNT Using Economic MPC, *Control*  
411 *Engineering Practice* 108 (2021) 104701.
- 412 [3] E. A. El Shenawy, Medhat Elkelawy, Hagar Alm-Eldin Bastawissi, Hitesh Panchal, Mahmoud M.  
413 Shams, Comparative study of the combustion, performance, and emission characteristics of a direct  
414 injection diesel engine with a partially premixed lean charge compression ignition diesel engines, *Fuel*  
415 249 (2019) 277-285.
- 416 [4] X. Chen, L. Liu, J. Zhang, J. Du, A Signal Processing of In-Cylinder Pressure for the Resonant  
417 Frequency Prediction of Combustion Process in Diesel Engines, ASME 2018 Internal Combustion  
418 Engine Division Fall Technical Conference, Volume 2: Emissions Control Systems; Instrumentation,  
419 Controls, and Hybrids; Numerical Simulation; Engine Design and Mechanical Development,  
420 ICEF2018-9534, San Diego, California, USA, November 4-7, 2018.
- 421 [5] J. Daniel, Y. Kok, F. Erik, K. Mattias, Combining Model-based Diagnosis and Data-driven Anomaly  
422 Classifiers for Fault Isolation, *Control Engineering Practice* 80 (2018) 146-156.
- 423 [6] A. Taghizadeh-Alisaraei, A. Mahdavian, Fault Detection of Injectors in Diesel Engines Using  
424 Vibration Time-frequency Analysis, *Applied Acoustics* 143 (2019) 48-58.
- 425 [7] C. Guardiola, B. Pla, P. Bares, A. Stefanopoulou, Cylinder Charge Composition Observation Based  
426 on In-cylinder Pressure Measurement, *Measurement* 131 (2019) 559-568.
- 427 [8] J. Zhao, J. Wang, On-Board Fuel Property Identification Method Based on High-Pressure Common  
428 Rail Pressure Signal, *Journal of Dynamics Systems, Measurement and Control* 136-3 (2014) 031010.

- 429 [9] F. Cheng, M. Ouyang, F. Yang, Real-time Start of Combustion Detection Based on Cylinder  
430 Pressure Signals for Compression Ignition Engines, *Applied Thermal Engineering* 114 (2017) 264-270.
- 431 [10] Joseph Gerard T. Reyes, Edwin N. Quiros, Determination of the Start and End of Combustion in a  
432 Direct Injection Diesel Engine Using the Apparent Heat Release Rate, ASME 2017 Power Conference  
433 Joint With ICOPE-17 collocated with the ASME 2017 11th International Conference on Energy  
434 Sustainability, the ASME 2017 15th International Conference on Fuel Cell Science, Engineering and  
435 Technology, and the ASME 2017 Nuclear Forum, Volume 1: Boilers and Heat Recovery Steam  
436 Generator; Combustion Turbines; Energy Water Sustainability; Fuels, Combustion and Material  
437 Handling; Heat Exchangers, Condensers, Cooling Systems, and Balance-of-Plant,  
438 POWER-ICOPE2017-3446, Charlotte, North Carolina, USA, June 26-30, 2017.
- 439 [11] T. Gao, S. Yu, K. Xie, M. Jeftic, M. Wang, M. Zheng, The Estimation of Nitrogen Oxides  
440 Reduction Potential Through Enhanced Heat Release Analysis, ASME 2016 Internal Combustion  
441 Engine Division Fall Technical Conference, ICEF2016-9440, Greenville, South Carolina, USA,  
442 October 9-12, 2016.
- 443 [12] P. Bares, D. Selmanaj, C. Guardiola, C. Onder, A new knock event definition for knock detection  
444 and control optimization, *Applied Thermal Engineering* 131 (2018) 80-88.
- 445 [13] A. Moosa, A. Farzad, A. Saeed, Z. Alireza, Classification-Based Fuel Injection Fault Detection of  
446 a Trainset Diesel Engine Using Vibration Signature Analysis, *Journal of Dynamics Systems,  
447 Measurement and Control* 142-5 (2020) 051003.
- 448 [14] Z. Yang, X. Han, S. Yu, X. Yu, M. Wang, M. Zheng, D. Ting, A Fuel Sensitive Ignition Delay  
449 Model for Direct Injection Diesel Engine Operating under EGR Diluted Conditions, SAE Technical  
450 Paper No. 2018-01-0231, 2018.
- 451 [15] R. Finesso, O. Marelllo, D. Misul, E. Spessa, M. Violante, Y. Yang, Gilles Hardy and Christian  
452 Maier, Development and Assessment of Pressure-Based and Model-Based Techniques for the MFB50  
453 Control of a Euro VI 3.0L Diesel Engine, *SAE International Journal of Engines* 10 (2017) 1538-1555.
- 454 [16] Y. Yang, Z. Peng, W. Zhang, G. Meng, Parameterised Time-frequency Analysis Methods and Their  
455 Engineering Applications: A Review of Recent Advances, *Mechanical Systems and Signal Processing*  
456 119 (2019) 182-221.

- 457 [17] Z. Feng, M. Liang, F. Chu, Recent Advances in Time–Frequency Analysis Methods for Machinery  
458 Fault Diagnosis: A Review with Application Examples, *Mechanical Systems and Signal Processing* 38  
459 (2013) 165-205.
- 460 [18] G. Purushottma, T. Rajiv, Multifault Diagnosis of Induction Motor at Intermediate Operating  
461 Conditions Using Wavelet Packet Transform and Support Vector Machine, *Journal of Dynamics*  
462 *Systems, Measurement and Control* 140-8 (2018) 081014.
- 463 [19] A.Taghizadeh-Alisaraei, B. Ghobadian, T. Tavakoli-Hashjin, S. S. Mohtasebi, M. Azadbakht,  
464 Characterization of Engine's Combustion-Vibration Using Diesel and Biodiesel Fuel Blends by  
465 Time-frequency Methods: A Case Study, *Renewable Energy* 95 (2016) 422-432.
- 466 [20] S. Ji, X. Lan, J. Lian, H. Wang, M.Li, Y. Cheng, W. Yin, Combustion Parameter Estimation for ICE  
467 from Surface Vibration using Frequency Spectrum Analysis, *Measurement* 128 (2018) 485-494.
- 468 [21] J.M. Luján, C. Guardiola, B. Pla, P. Bares, Estimation of Trapped Mass by In-cylinder Pressure  
469 Resonance in HCCI Engines, *Mechanical Systems and Signal Processing* 66-67 (2016) 862-874.
- 470 [22] C. Guardiola, B. Pla, P. Bares, A. Barbier, An Analysis of the In-cylinder Pressure Resonance  
471 Excitation in Internal Combustion Engines, *Applied Energy* 228 (2018) 1272-1279.
- 472 [23] V. Dekys, P. Kalman, P. Hanak, P. Novak, Z. Stankovicova, Determination of Vibration Sources by  
473 Using STFT, *Procedia Engineering* 177 (2017) 496-501.
- 474 [24] A. Ferrari, F. Paolicelli, A Virtual Injection Sensor by Means of Time Frequency Analysis,  
475 *Mechanical Systems and Signal Processing* 116 (2019) 832-842.
- 476 [25] K. Ishiduka, K. Uchiyama, K. Higuchi, N. Yamada, K. Takeuchi, Herrmann OE, et al., Further  
477 Innovations for Diesel Fuel Injection Systems: Close-loop Control of Fuel Quantity by i-Art & Ultra  
478 High Injection Pressure, 19th Aachen colloquium, 2010.
- 479 [26] J.Hammer, M. Raff , D. Naber, Advanced Diesel Fuel Injection Equipment - A Never Ending  
480 BOSCH Story, 14th Internationales Stuttgarter Symposium, Springer Vieweg, Wiesbaden, Germany,  
481 2014.
- 482 [27] P. Voigt, H. J. Schiffgens, C. Daveau, J. C. Oge, J. L. Beduneau, G. Meissonnier, C. Tapin, X. Lale,  
483 Delphi Injector Closed Loop Control Strategy Using the “Switch” Technology for Diesel Passenger  
484 Cars – Injector Hardware. 10. Tagung Diesel- und Benzindirekteinspritzung 2016. Wiesbaden: Springer

485 Vieweg; 2016. p. 41–66.

486 [28] A. Ferrari, C. Novara, E. Paolucci, O. Vento, M. Violante, T. Zhang, Design and Rapid Prototyping  
487 of a Closed-loop Control Strategy of the Injected Mass for the Reduction of CO<sub>2</sub>, Combustion Noise  
488 and Pollutant Emissions in Diesel Engines, *Applied Energy* 232 (2018) 358-367.

489 [29] A. Ferrari, C. Novara, E. Paolucci, O. Vento, M. Violante, T. Zhang, A New Closed-loop Control of  
490 the Injected Mass for a Full Exploitation of Digital and Continuous Injection-rate Shaping, *Energy*  
491 *Conversion and Management* 177 (2018) 629-639.

492 [30] A. Ferrari, T. Zhang, Benchmark between Bosch and Zeuch Method-Based Flowmeters for the  
493 Measurement of the Fuel Injection Rate, *International Journal of Engine Research* (2019) In press.

494 [31] A. E. Catania, A. Ferrari, E. Spessa, Temperature variations in the simulation of high-pressure  
495 injection-system transient flows under cavitation, *International Journal of Heat and Mass Transfer* 51  
496 (2008), 2090-2107.

497 [32] Ferrari A., Mittica A., Thermodynamic formulation of the constitutive equations for solids and  
498 fluids, *Energy Conversion and Management* 66 (2016), 77-86.

499 [33] Payri, R., F. Salvador, M. Carreres and J. D. L. Morena. “Fuel temperature influence on the  
500 performance of a last generation common-rail diesel ballistic injector. Part II: 1D model development,  
501 validation and analysis.” *Energy Conversion and Management* 114 (2016): 376-391.

502 [34] F. J. Salvador, J. Gimeno, M. Carreres, M. Crialesi-Esposito, Fuel Temperature Influence on the  
503 Performance of a Last Generation Common-Rail Diesel Ballistic Injector. Part I: Experimental Mass  
504 Flow Rate Measurements and Discussion, *Energy Conversion and Management* 114 (2016), 364-375.

505 [35] C. Öztürk, Development of Experimental Techniques to Minimise the Leakage Errors Involved in  
506 FFT based Measurements, *Applied Acoustics* 44-4 (1995), 375-382.

507 [36] Ferrari, A. and O. Vento. “Influence of Frequency-Dependent Friction Modeling on the Simulation  
508 of Transient Flows in High-Pressure Flow Pipelines.” *Journal of Fluids Engineering-transactions of The*  
509 *Asme*, 142 (2020).

510 [37] Q. Fang, J. Fang, J. Zhuang, Z. Huang, Influences of Pilot Injection and Exhaust Gas Recirculation  
511 (EGR) on Combustion and Emissions in a HCCI-DI Combustion Engine, *Applied Thermal Engineering*  
512 48 (2012) 97-104.

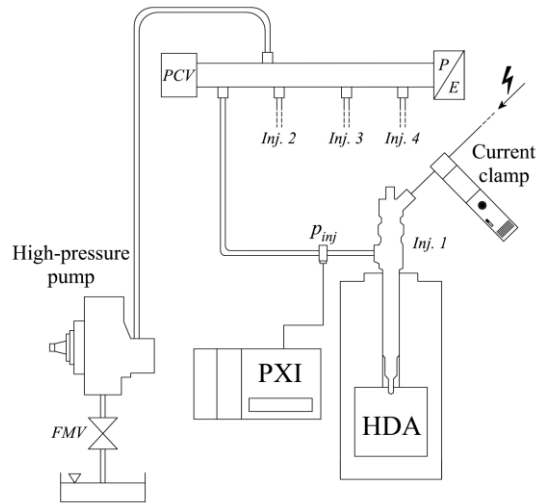


**Figure 1. The experimental layout of the injection system**

513

514

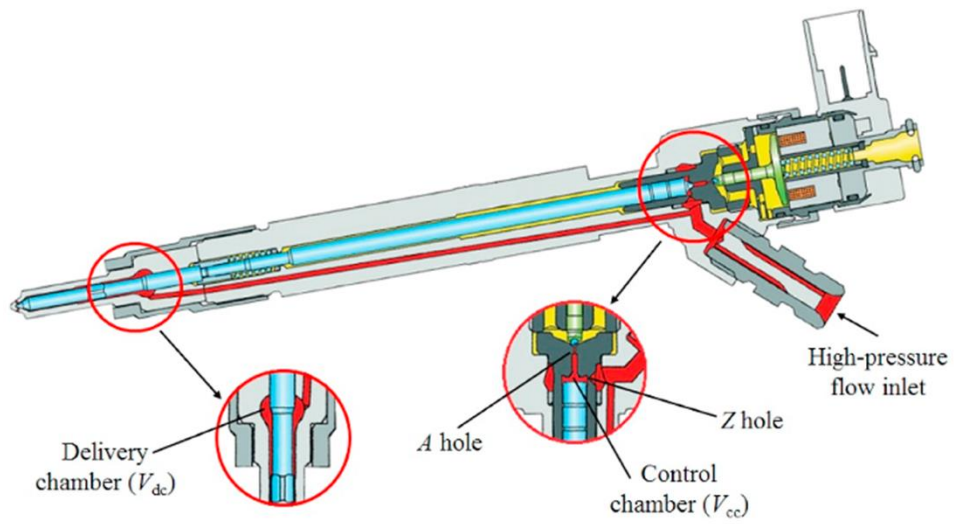


**Figure 2. CRI 2.18 solenoid injector**

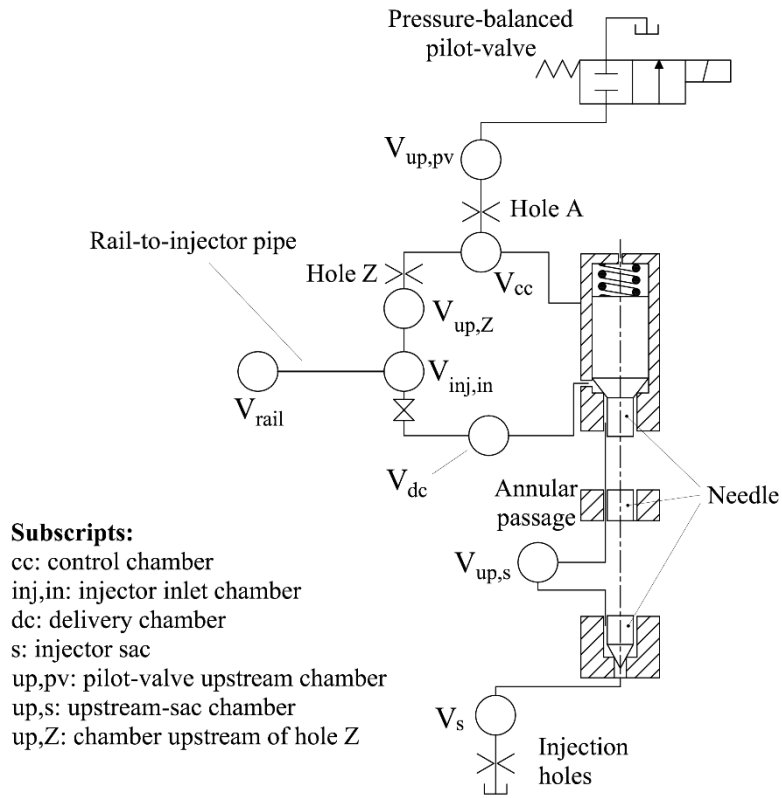


Figure 3. Schematic of the hydraulic circuit of the injection system

515

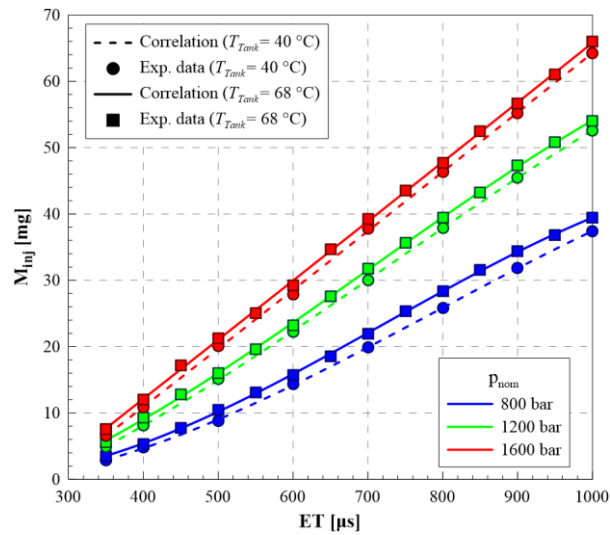


Figure 4. Injector characteristics for different  $p_{nom}$  and  $T_{tank}$  values

516

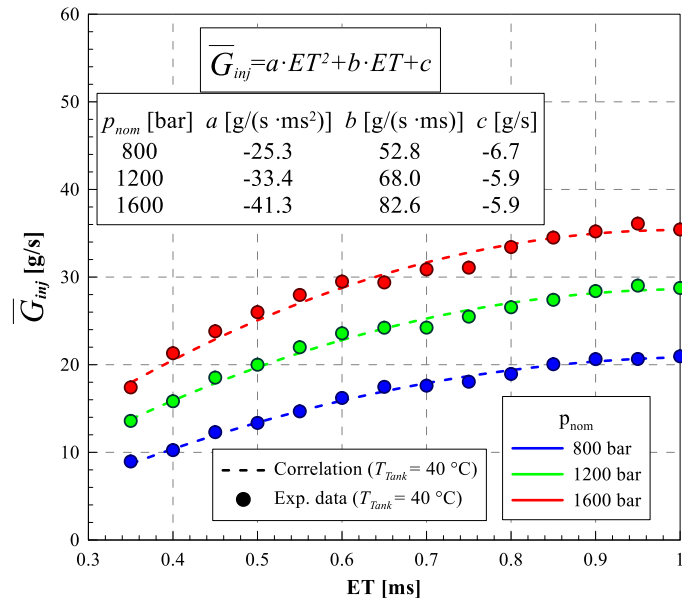
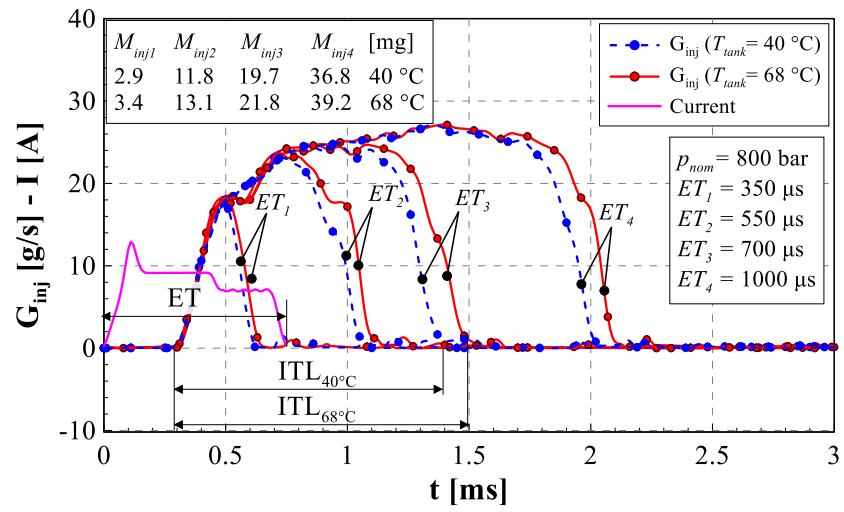
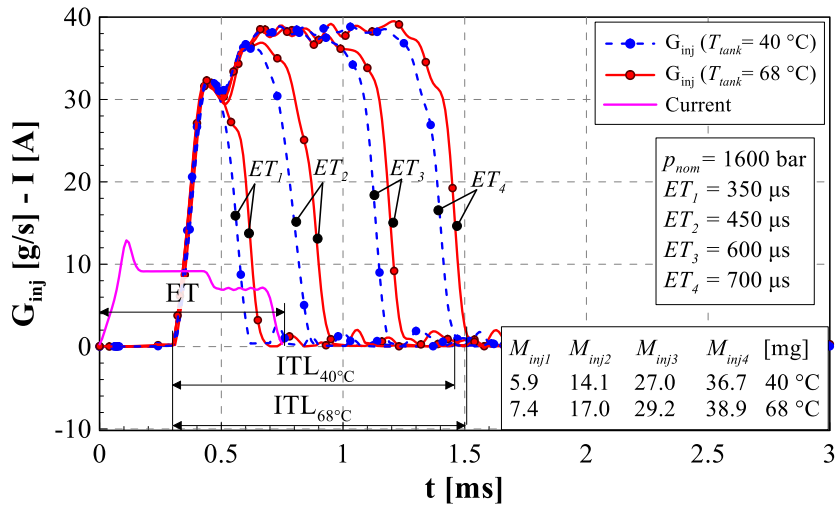


Figure 5. The mean injected flow-rate with respect to  $ET$  for different  $p_{nom}$  values



(a)



(b)

Figure 6. Effect of the tank fuel temperatures on the injected flow-rate for different  $ET$  values.

(a):  $p_{nom} = 800$  bar (b):  $p_{nom} = 1600$  bar

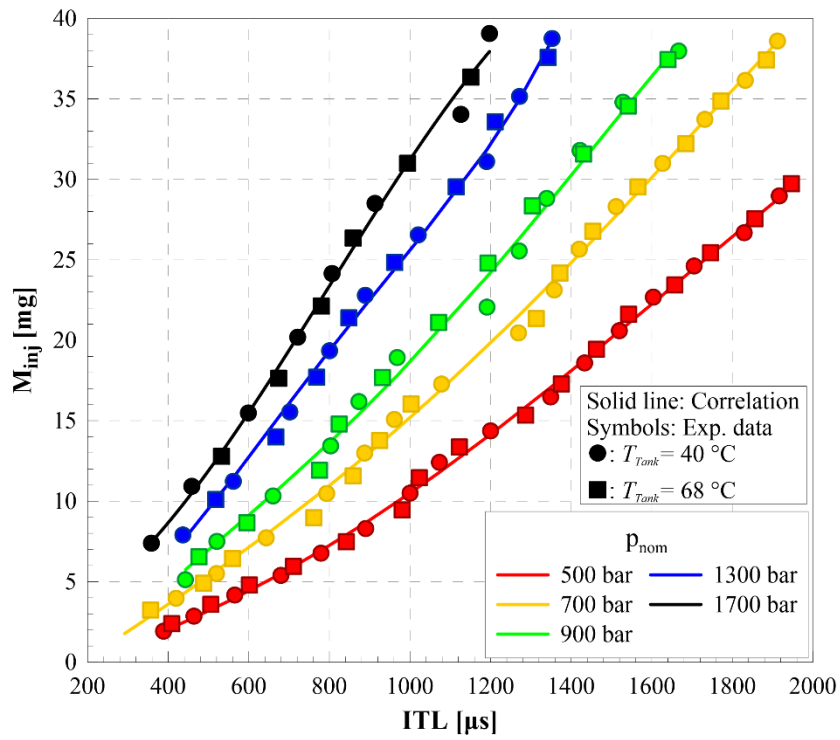


Figure 7.  $ITL-M_{inj}$  injector characteristic for different  $p_{nom}$  and  $T_{tank}$  values

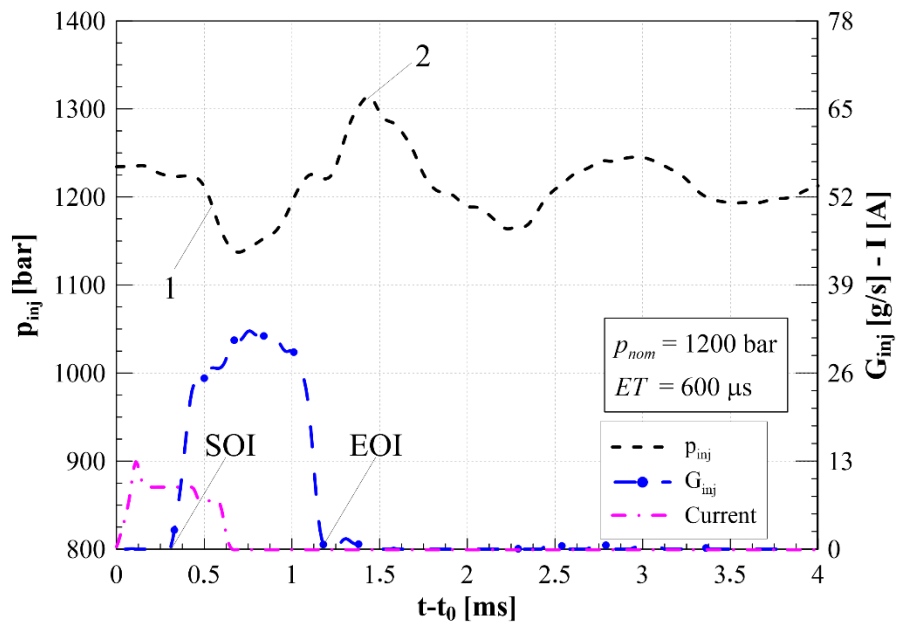


Figure 8.  $G_{inj}(t)$ ,  $p_{inj}(t)$  and electrical current for  $p_{nom}=1200$  bar and  $ET=600$   $\mu s$

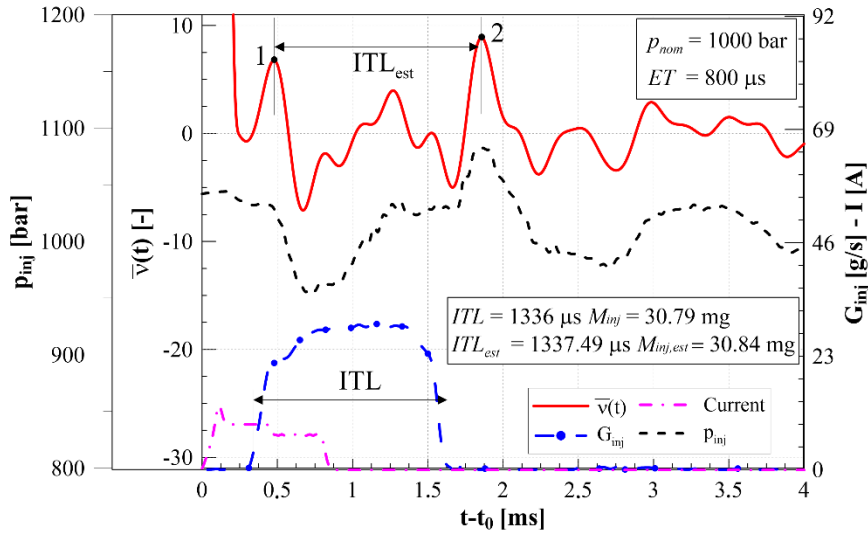


Figure 9.  $G_{inj}(t)$ ,  $p_{inj}(t)$  and the normalized  $MIF$  for  $p_{nom}=1000$  bar and  $ET=800 \mu s$  ( $T_{tank}=40 \text{ }^\circ\text{C}$ )

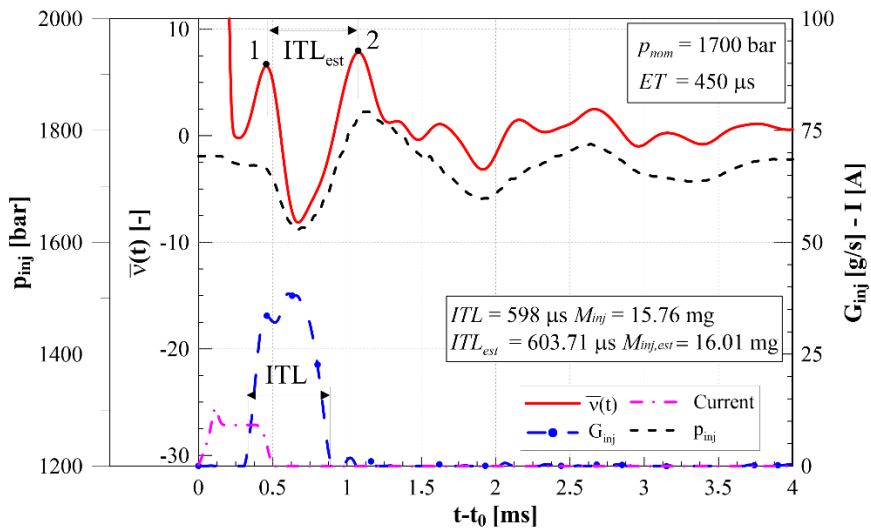


Figure 10.  $G_{inj}(t)$ ,  $p_{inj}(t)$  and the normalized  $MIF$  for  $p_{nom}=1700$  bar and  $ET=450 \mu s$  ( $T_{tank}=40 \text{ }^\circ\text{C}$ )

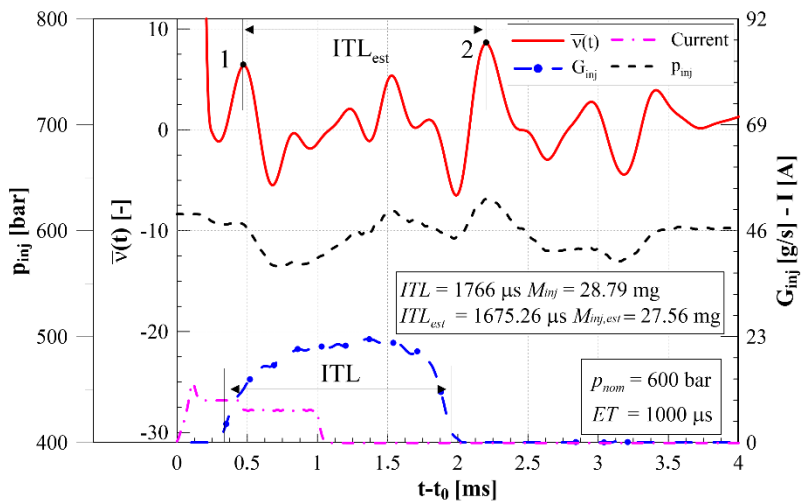
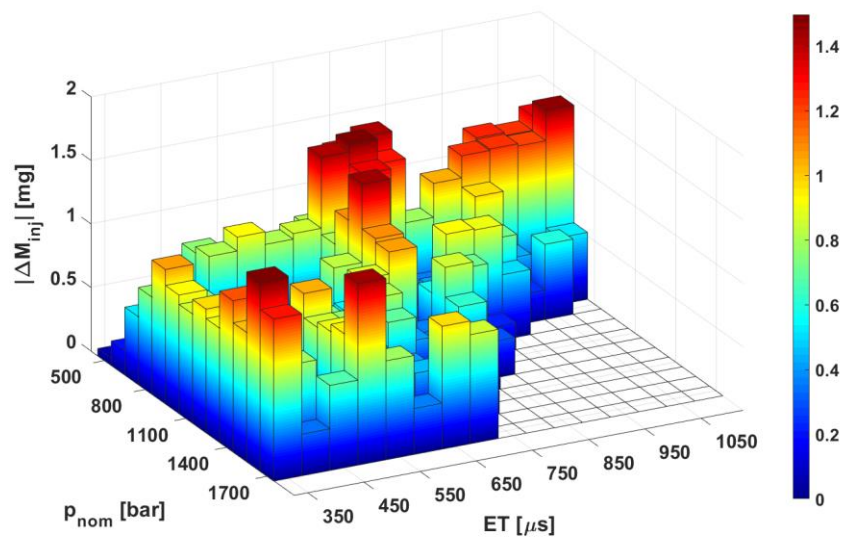
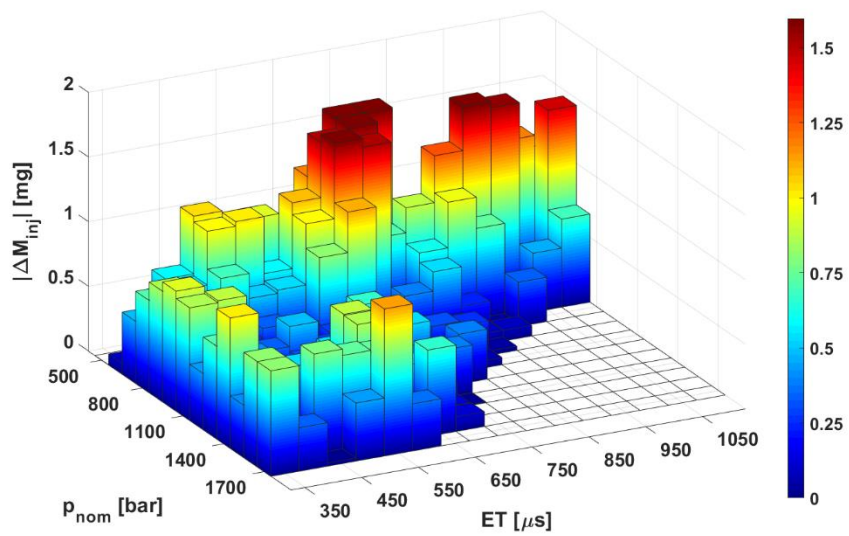


Figure 11.  $G_{inj}(t)$ ,  $p_{inj}(t)$  and the normalized  $MIF$  for  $p_{nom}=600$  bar and  $ET= 1000 \mu s$  ( $T_{tank}=40 \text{ }^\circ\text{C}$ )

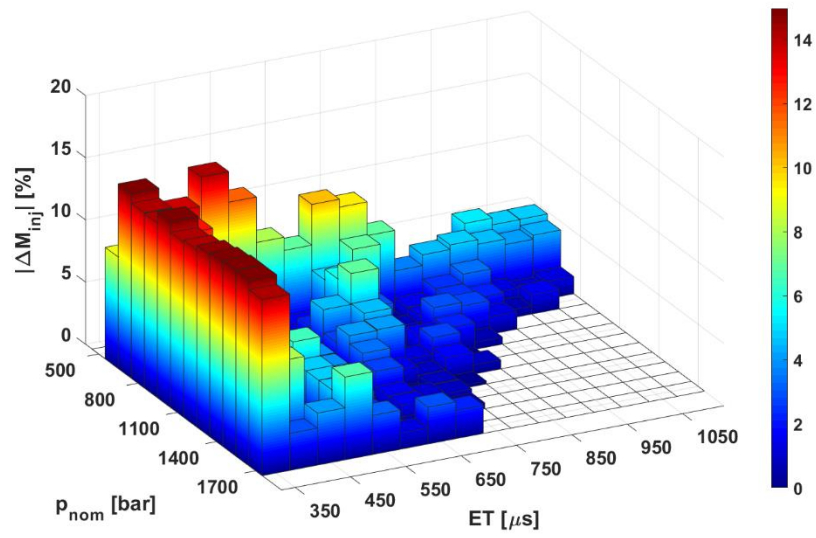


(a)

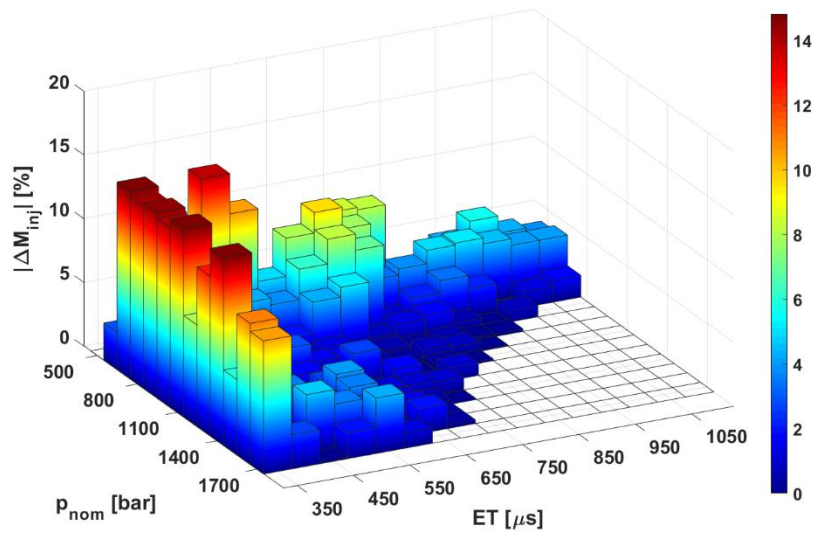


(b)

Figure 12. Injected mass prediction accuracy (a:  $T_{tank} = 40$  °C, b:  $T_{tank} = 68$  °C)



(a)



Injected mass prediction percentage error (*a*:  $T_{tank}=40\text{ }^{\circ}\text{C}$ , *b*:  $T_{tank}=68\text{ }^{\circ}\text{C}$ )

535

536

537

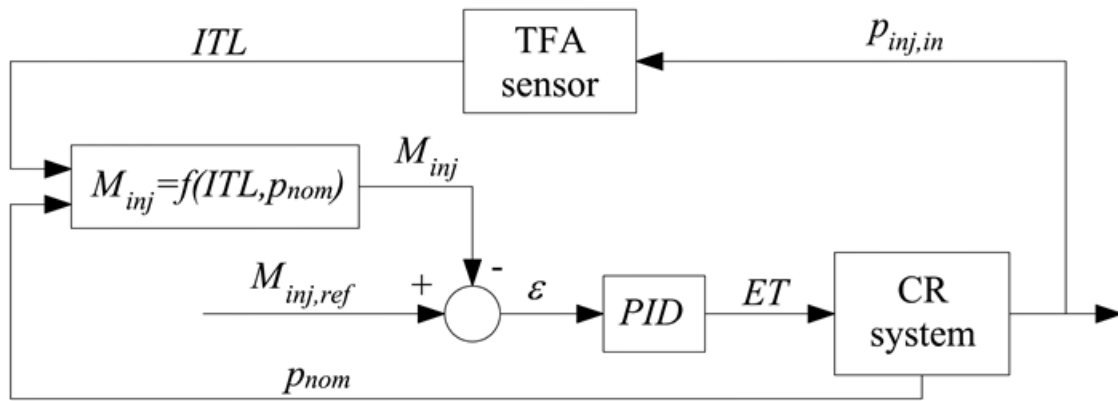


Figure 14. The implemented closed-loop strategy based on *TFA* analysis